

# A ‘simple metal’ description of liquid carbon, its warm-dense matter states, and the identification of liquid-liquid phase transitions.

M. W. C. Dharma-wardana<sup>1,\*</sup> and Dennis D. Klug<sup>2</sup>

<sup>1</sup>*National Research Council of Canada, Ottawa, Ont. Canada K1A 0R6*

<sup>2</sup>*National Research Council of Canada, Ottawa, Ont. Canada K1A 0R6*

(Dated: July 6, 2021)

Liquid carbon is a complex fluid whose theory is claimed to require explicit covalent interactions and many-center potentials. Thus very expensive  $N$ -atom quantum simulations for  $N \sim 100 - 500$  using density-functional theory (DFT), and molecular-dynamics (MD) are usually deployed. They show intriguing structure factors with a split first peak and features not found in simple metallic liquids. We show that a *simple-metal* model using only one-body electron densities, one-body ion densities, and appropriate exchange-correlation functionals implemented in the one-atom DFT approach of the neutral pseudo-atom (NPA) model, quantitatively and inexpensively recovers the results of  $N$ -atom DFT simulations. We show that structural changes are dominated by strong electron-ion interactions at the Fermi energy. Evidence is presented for three liquid-liquid phase transitions in the 3 to 4 g/cm<sup>3</sup> range using NPA calculations supported by DFT-MD simulations.

PACS numbers: 62.50.-p, 52.25.Fi, 81.05U-, 78.70.Ck

*Introduction* - Many light elements such as H, B, C, N, Si, P, and their mixtures form strong covalency in the solid. They seem to retain some of this bonding on melting [1–4] and even in warm-dense-matter (WDM) regimes [5–9]. A theory for reliably and inexpensively predicting the properties of these materials is needed in technological applications. Their properties under high densities  $\bar{\rho}$  and temperatures  $T$  are needed in high-energy density physics [10, 11] and astrophysics [12–14]. Besides technological interests, the quantum theory of its liquid state has provoked great interest since the 1980s [1, 9].

We focus on basic issues of wider interest and the intriguing interactions in “tetrahedral fluids”, typified by liquid carbon ( $l$ -C) where such effects are strongest. A large effort, using chemical bonding models treat these electron-ion systems *via* multi-center ion-ion potentials, with the electron subsystem integrated out. Within such models, pair-potentials cannot stabilize diamond structures without at least “three body forces”, as in, say, the Stillinger-Weber model [16].

This paradigm uses potentials with hundreds of parameters fitted to data covering wide ranging densities  $\bar{\rho}$ , temperatures  $T$  and structures. Yet, even a model for liquid aluminum at finite  $T$ , a trivial problem in standard liquid-metal theory, requires over forty parameters in current effective medium theories [17]. Nevertheless, these multi-center potentials give disappointing results for liquid carbon [7]. Glossli *et al.* [3] using the Brenner potential found a liquid-liquid phase transition (LPT) between a  $sp^3$  bonded high density liquid and an  $sp, sp^2$  bonded low density liquid. However, a DFT-MD study using the Perdew-Burke-Ernzerhof (PBE) exchange-correlation (xc) functional [22] found no such LPT [3, 23]. Here we report LPTs revealed by one-center DFT methods and confirmed by standard  $N$ -center DFT-MD simulations.

The DFT-MD method implemented in codes, e.g., VASP [25] or ABINIT [24] will be denoted ‘Quantum MD’ (QMD) for brevity. It treats the liquid as an average over many realizations of a periodic cluster of  $N$ -atoms in the simulation cell. It is an  $N$ -center DFT for an  $N$ -center electron density  $n(\vec{r}, \vec{R}_1, \dots, \vec{R}_N)$ . Such complex densities are sensitive to the electron xc-functional used. Remsing *et al.* [26] showed that the VASP results for  $l$ -Si from the PBE functional differed significantly from those of the ‘strongly constrained and appropriately normed’ (SCAN) functional [27]. Expensive force-matching methods [17, 28] and decompositions of  $N$ -body properties [18, 19] are needed to extract individual atomic or pair properties from QMD calculations.

According to Hohenberg and Kohn, one-body densities of electrons and ions are sufficient for a complete thermodynamics of *any* electron-ion system. A one-atom DFT is utilized in the neutral-pseudo-atom (NPA) method used here. It is an ‘average-atom’ model [20, 21], but not restricted to high  $T$ . It was recently used for super-cooled  $l$ -Si, a complex ‘tetrahedral’ liquid [30, 31, 33]. The many-ion and many-electron effects are included in the NPA via suitable ion-ion, electron-electron and electron-ion exchange-correlation (xc) functionals of the one-body electron density  $n(\vec{r})$  and the one-body ion density  $\rho(\vec{r})$  [32, 34].

Unlike the  $\text{Si}^{4+}$  ion with a robust core, the point-like  $\text{C}^{4+}$  ion produces strong interactions, especially in the low- $\bar{\rho}$ , low- $T$  region. Stanek *et al.* [28] showed that the use of linear-response (LR) potentials generated from NPA for  $l$ -C at the “graphite density”  $\rho_G \simeq 2.267\text{g/cm}^3$  at low  $T$  strongly over-estimated the first peak in the NPA pair distribution function (PDF). Linear responses is known to fail for expanded metals at low  $T$ .

In the NPA a carbon nucleus is at the origin of  $l$ -carbon, a *uniform system* with a free electron density  $\bar{n}$ . It acquires a bound electron density  $n_b(r)$  within its Wigner-Seitz sphere of radius  $r_{\text{ws}}$ , a free electron distri-

\* Email address: chandre.dharma-wardana@nrc-cnrc.gc.ca

bution  $n_f(r)$  and an ion distribution  $\rho(r)$  covering the whole volume, with a mean density  $\bar{\rho}$ .

QMD and NPA calculations show that the average ionization  $\bar{Z} = 4$  for the  $\bar{\rho}, T$  studied here [1, 5]. The C-C bonds (single, double etc.,) have a bond energy  $E_b$  of the order of  $\sim 4\text{-}8$  eV [35]. However, a WDM medium containing free electrons produces screening effects causing the band gap to close on melting, with the conductivity and reflectivity sharply increasing. However, a peak at the C-C distance of  $1.4 \text{ \AA}$  is found in the  $g_{cc}(r)$  QMD simulations [1] and even in early NPA calculations [9].

The NPA calculation provides the free electron density  $n_f(r)$  and the excess free electron density  $\Delta n_f(r) = n_f(r) - \bar{n}$  at a carbon ion carrying its bound shell of electrons, as discussed in more detail in SM[29] which is given here as an Appendix. The Fourier transform  $\Delta n_f(k)$  serves to construct pair potentials.

*Pseudopotentials and pair potentials in l-C* – The  $N$ -center QMD calculations provide an  $N$ -center potential energy surface used to construct force-matched pair-potentials. The electrons have been eliminated from such potentials [17]. In contrast, the NPA treats a two-component system of electrons and ions, and forms a pseudopotential  $U_{ei}(k)$  for the specified  $\bar{n}, T$  (see Fig. 1). The simplest local linear-response (LR) potential is:

$$U_{ei}(k) = \frac{\Delta n_f(k)}{\chi(k, \bar{n}, T)}, \quad U_{ei}(k) = -ZV_k M_k, \quad (1)$$

Here  $\chi(k)$  is the linear response of the interacting electron fluid at  $\bar{n}, T$ , discussed further in the Appendix given as Supplemental Material [29]. The Coulomb potential  $V_k$  and the form factor are  $4\pi/k^2$ ,  $M_k$  respectively. The pseudopotential is in LR, but  $\Delta n_f(k)$  has all the non-linear effects of the Kohn-Sham calculation. The nonlinearities in the fluid response are not treated as the response function  $\chi(k)$  is based on plane waves. The limits of validity of the LR  $U_{ei}(k)$  are discussed in Ref. [36]. It fails for low  $\bar{\rho}, T$  when non-linear effects prevail.

In Fig. 1(a) we display the pseudopotential for a range of densities, for  $T = 1$  eV. With  $Z = 4$ ,  $l\text{-C}$  is a dense electronically degenerate metal even at 1 eV, even for  $2.5\text{ g/cm}^3$  when  $r_s \simeq 1.48$  and  $E_F \simeq 23$  eV. Essentially all electron-ion scattering occurs at the Fermi energy  $E_F$ , with a momentum transfer  $q = 2k_F$ , where  $K_F$  is the Fermi momentum.

A sharp change in  $M_k$  occurs just below  $5\text{ g/cm}^3$  as seen from Fig. 1(a). Then, near the ‘diamond density’  $\rho_D$ , viz.,  $\simeq 3.52\text{ g/cm}^3$   $M_k$  at  $k = 2k_F$  passes through zero and changes sign (curve with circles). This suggests that the LR  $U_{ei}(k)$ , Eq. 1, begins to fail for  $\bar{\rho} \leq \rho_D$  even though the electron density is high. However, we display the linear-response  $U_{ei}(k)$  and the calculated  $S(k)$  even for densities below  $\rho_D$  in Fig. 1, as they indicate when non-linear effects become important in the range  $\rho_D > \bar{\rho} \geq \rho_G$ . Figure 1 shows that LR is unacceptable below  $\bar{\rho} \sim 3 \text{ g/cm}^3$  and  $T = 1$  eV.

The LR pseudopotential defines a pair potential in

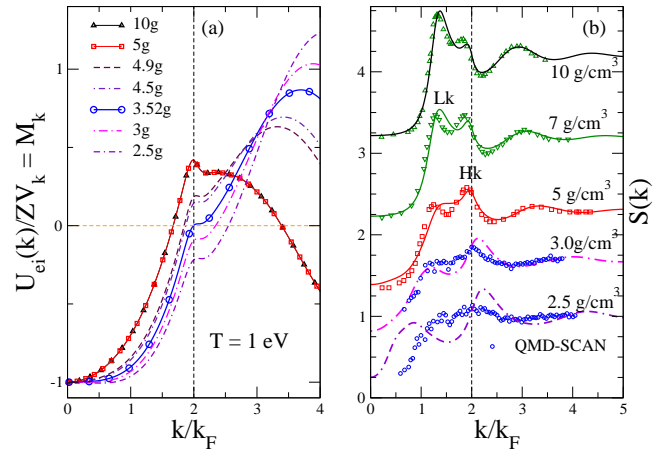


FIG. 1. (Color online) (a) The LR-NPA pseudopotential  $U_{ei}(k)$  from Eq. 1 for  $l$ -carbon at 1 eV for  $2.5\text{ g/cm}^3 \leq \bar{\rho} \leq 10\text{ g/cm}^3$ . The  $U_{ei}$  is invariant between  $5\text{-}10\text{ g/cm}^3$  and a sharp change occurs below  $5\text{ g/cm}^3$ . The  $U_{ei}(k = 2k_F) \rightarrow 0$  at  $\rho_D \simeq 3.5\text{ g/cm}^3$  (line with circles). Panel (b) shows typical  $S(k)$  using the LR- $U_{ei}(k)$  and the electron fluid response function  $\chi_{ee}(k, T, \bar{n})$ . The unconnected symbols for  $\bar{\rho} \geq 5\text{ g/cm}^3$  are the QMD  $S(k)$  of Ref. [5] using the PBE functional. The smooth curves are NPA calculations. The high- $K$  subpeak (marked Hk) falls on  $2k_F$  for  $\bar{\rho} \geq 3\text{ g/cm}^3$ . We compare the LR-NPA  $S(k)$  and QMD-SCAN  $S(k)$  at  $3 \text{ g/cm}^3$ , and  $2.5 \text{ g/cm}^3$  showing that LR-NPA is unacceptable below  $3 \text{ g/cm}^3$ .

second-order perturbation theory:

$$V_{ii}(k) = Z^2 V_k + |U_{ei}(k)|^2 \chi(k, r_s, T) \quad (2)$$

This implies that at  $\rho_D$  the pair potential at  $2k_F$  becomes just  $Z^2 V_{k_F}$  since  $M_{2k_F} = 0$ . The pair potential is that of two *unscreened* carbon ions if non-linear effects are neglected. Our NPA and QMD calculations detect an LPT very near this density.

The ion distribution  $\rho(r) = \bar{\rho}g(r)$  is given by the ion-DFT equation using the pair-potential  $V_{ii}(r)$  and the ion-ion xc-functional. This amounts to solving a hypernetted-chain (HNC) equation containing a bridge function [32], to yield the  $g(r)$  and the  $S(k)$  of the ion subsystem. In Fig. 1(b) we compare the NPA and QMD results of Ref. [5] where the PBE xc-functional has been used.

The first peak of  $S(k)$  displays lower- $k$  (Lk) and higher- $k$  (Hk) subpeaks. The interactions occur via strong electron scattering at the Fermi surface, with a momentum transfer of  $q = 2k_F$ . The fluid responds by creating the high- $k$  peak Hk as close to  $2k_F$  as possible for fluids with  $\bar{\rho} > \sim 3 \text{ g/cm}^3$  as shown in panel (b). This occurs if enough atoms occupy the first turning point of the Friedel oscillations of the pair-potential, while excess atoms move to the lower- $k$  (i.e., more distant) weaker minima, and vice versa depending on the fluid density.

The electron xc-energy favours a high-density electron fluid, i.e., a shell of atoms even in a positive energy ledge of the pair-potential (Fig. 2). This is less advantageous

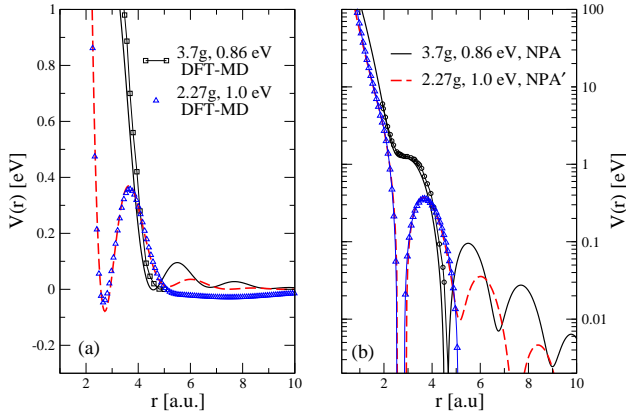


FIG. 2. Color online (a) A comparison of the C-C pair potentials from a force-matched DFT-MD calculations at  $\rho_3=3.27\text{g}/\text{cm}^3$  [6] with the NPA pair potential in LR. The force-matched DFT-MD potentials fail to recover the higher Friedel oscillations (for  $r > 5$  a.u.) seen in the NPA potentials. (b) The same data are shown on a log-scale (y-axis). The maximum of the  $g(r)$  at this density corresponds to the positive energy ledge for this range of densities. The extent of the agreement of the the  $g(r)$ ,  $S(k)$  from the NPA and the QMD simulation [6] for this case was discussed in Ref. [37]

at lower density and the peak Hk at  $2k_F$  grows at the expense of Lk, as seen in Fig. 1. The LR-pseudopotential at  $2k_F$ , i.e.,  $U_{ei}(2k_F)$  becomes zero at about the diamond density,  $\rho_D \sim 3.5\text{g}/\text{cm}^3$ , and changes sign for lower densities. Coherent scattering from atoms positioned in the Friedel minima contribute coherently to the subpeak Hk in  $S(k)$  at  $2k_F$ . This coherence links the coordination number with the liquid phases of a homogeneous fluid.

The ion distribution modifies itself to minimize the energy of the system in two ways: (i) its Hk peak locates itself as closely as possible to  $2k_F$ . (ii) At densities below  $\rho_D$ , the first atomic shell attempts to still retain a high coordination number  $N_c$  at the expense of outer shells. Even when  $\bar{\rho}$  is low, the *local density* of the fluid adjusts to bring Hk to  $2k_F$ , lowering the free energy via strong scattering at  $E_F$ . That is, atoms may be drawn towards the central ion by decreasing the depths of secondary Friedel minima. This is favourable for  $N_c \geq 6$ .

*Evidence for LPTs in liquid carbon.* Here we limit ourselves to the  $\bar{\rho} \geq 2.9\text{g}/\text{cm}^3$  range where the LR forms for  $U_{ei}(k)$ ,  $V_{ii}(k)$ ,  $S(k)$  etc., adequately agree with QMD results without non-LR modifications. We examine the pressure and the compressibility for signs of LPTs using the NPA for  $\bar{\rho} > 2.9\text{g}/\text{cm}^3$ , thus excluding the low  $\bar{\rho}$  explored in Ref. [38]. We find three LPTs labeled LPT<sub>3</sub>, LPT<sub>3.5</sub>, and LPT<sub>3.75</sub>, as they occur at  $\bar{\rho} \simeq 3.15$ , 3.5, and 3.75 g/cm<sup>3</sup> in the NPA calculations. The QMD results confirm them, at slightly shifted  $\bar{\rho}$  values. Thus the LPT<sub>3.5</sub> occurs at 3.42g/cm<sup>3</sup> in the QMD-SCAN data.

Figure 3(a) displays the pressure from the  $N$ -atom QMD calculation of Ref. [5], using  $N = 196$  to 256 atoms and the PBE xc-functional. Our QMD calculation for  $\bar{\rho} < 4\text{g}/\text{cm}^3$  using the SCAN functional with  $N = 108$

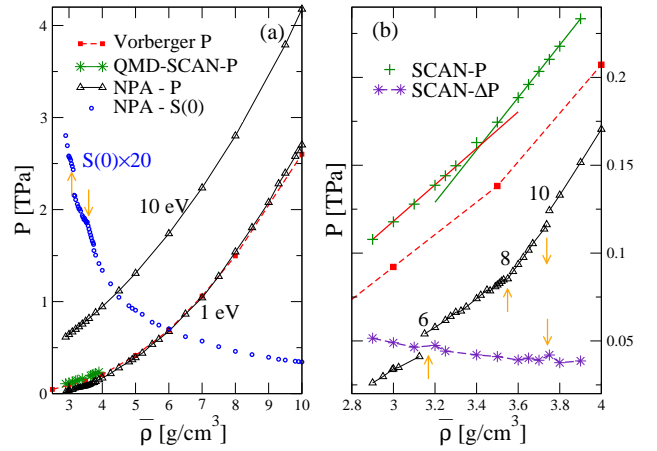


FIG. 3. (Color online) (a) The pressure at 1 eV from QMD-PBE [5], QMD-SCAN and NPA calculations. The  $k \rightarrow 0$  of  $S(k)$ , viz.,  $S(0) = \kappa/\kappa^0$  where  $\kappa$  is the isothermal compressibility displays discontinuities (arrows) at the  $P$ -discontinuities. The pressure at 10 eV shows no discontinuities. (b) The discontinuities in the NPA pressure at 1 eV support three LPTs at  $\bar{\rho} \sim 3.15$ ,  $\sim 3.52$ , and 3.75 g/cm<sup>3</sup>. The data points above and below  $\bar{\rho} \simeq 3.42\text{g}/\text{cm}^3$  from QMD-SCAN accurately fall on straight lines intersecting at  $\bar{\rho} \simeq 3.42\text{g}/\text{cm}^3$  if a single Gaussian is fitted to the QMD  $P$ -distributions. However, the spread of the SCAN-QMD  $P$  distributions (labeled SCAN- $\Delta P$ ,  $\times 3.3$ ) increase (arrows) at LPT<sub>3</sub> and LPT<sub>3.75</sub> and use a two-Gaussian fit (see Fig. 4).

atoms is also shown. The NPA, PBE and SCAN calculations of  $P$  differ by about the same magnitude in this region. It also displays the NPA pressure and the isothermal compressibility via the limit  $S(k \rightarrow 0)$ , i.e.,  $S(0) = \kappa/\kappa^0$ . Here  $\kappa^0 = 1/\bar{\rho}T$  is the ideal fluid compressibility. The  $S(0)$  calculation is independent of the pressure calculation. Hence discontinuities in the pressure, and in  $S(0)$  independently support one another. The  $P$  data at 10 eV show no discontinuities.

Fig 3(b) displays the  $2.9 \leq \bar{\rho} \leq 4\text{g}/\text{cm}^3$  range. The QMD-SCAN pressure confirms the LPT<sub>3.5</sub> seen in the NPA, while the other two LPTs seen in the NPA require a deeper examination of the QMD-SCAN pressure data.

The fluctuations in the pressure within an equilibrated MD run fall on a Gaussian distribution (see SM[29], i.e., the Appendix) for a uniform fluid. The width of  $P$  fluctuations in the QMD-SCAN (labeled SCAN- $\Delta P$ ) change significantly near the discontinuities (vertical arrows, Fig. 3) at LPT<sub>3</sub> and LPT<sub>3.75</sub>. It is found that the  $P$  distributions at LPT<sub>3</sub> and LPT<sub>3.75</sub> are best fitted with two Gaussians instead of one, giving two pressure peaks (Fig.4). At LPT<sub>3.5</sub> the distribution is not bimodal (see SM, or Appendix). Thus at 3.1g/cm<sup>3</sup>, two contributions at 70% and 30% give the average QMD-SCAN  $P$  shown in Fig. 3. The need for two-Gaussians at LPT<sub>3</sub> and LPT<sub>3.75</sub> to describe the QMD  $P$  confirms the NPA pressure discontinuities for a uniform fluid. QMD averages over clusters, does not demand microscopic uniformity, and fails to reveal these LPTs explicitly.

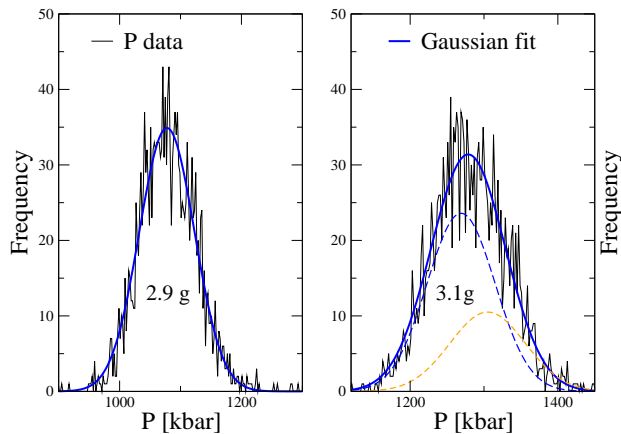


FIG. 4. The  $P$ -distribution from QMD-SCAN calculations. (a)  $2.9\text{g/cm}^3$  and (b)  $3.1\text{g/cm}^3$ , at  $\text{LPT}_3$ . While the  $2.9\text{g/cm}^3$  case fits to one Gaussian, that at  $3.1\text{g/cm}^3$  is best fitted with two Gaussians, implying an inhomogeneous plasma at the LPT. This is also the case for  $\text{LPT}_{2.5}$  but the  $\text{LPT}_{2.5}$  is

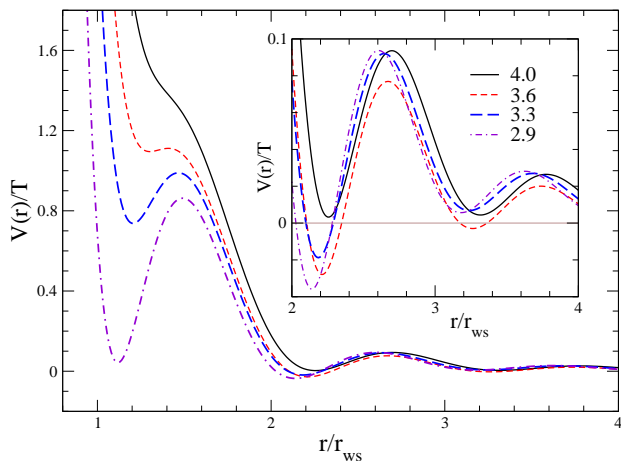


FIG. 5. C-C pair potentials at densities in regions separated by the discontinuities in the NPA pressure. The densities shown ( $4, 3.6, 3.3, 2.9\text{g/cm}^3$ ) are for regions where the coordination numbers  $N_c \sim 10, 8, 6$ , and  $N_c < 6$  prevail. The discontinuities imply LPTs in the NPA calculation. The QMD data imply an LPT separating the  $N_c = 6$  and  $8$  regions.

There are corresponding discontinuities in  $S(0)$  since the fluid compressibility changes sharply at the LPTs, while  $\bar{Z}$  remains constant. Astrophysics studies [13] of carbon even at  $100\text{eV}$  have shown discontinuities near  $\bar{\rho} \sim 3\text{g/cm}^3$  in several physical properties.

*Discussion* – The  $S(k)$  data have shown that the ionic structure of the fluid is determined by strong electron scattering across the Fermi surface, and by the Friedel oscillations of the pair-potentials. This ‘Coulomb fluid’ model of  $l$ -carbon provides a complete account of the structural and thermodynamic properties of  $l$ -carbon without invoking covalent bonds, using only simple LR pair-potentials. The covalent bonds are mere transient

bonds, lasting the life-time of longitudinal phonons, while DFT deals with thermodynamic ( $\omega \rightarrow 0$ ) averages.

The LPTs implied by the discontinuities in  $P$  and in  $\kappa$  seen in Fig. 3 in NPA occur near densities  $\sim 3.15, 3.54, 3.75\text{g/cm}^3$  at  $1\text{eV}$ , with the coordination number  $N_c$  changing to  $6, 8$ , and  $10$  respectively (see SM, i.e., Appendix). The  $\text{LPT}_{3.5}$  near  $\bar{\rho}_D, N_c = 8 \rightarrow 6$  is clearly seen in the QMD-SCAN  $P$  data that accurately fall on two straight lines crossing at  $3.42\text{g/cm}^3$ . The change in  $N_c$  follows a change in the sign of the NPA pseudopotential at the diamond density, when  $U_{ei}(2k_F)$  becomes zero.

The three LPTs occur while the fluid conserves the structure of  $S(k)$  near  $2k_F$  at each change of  $N_c$ , while  $\bar{Z}$  also remains constant. Hence the conductivity may be continuous across these LPTs. However, a slight discontinuity is seen at the  $\text{LPT}_{3.5}$  as discussed in the SM (i.e., Appendix) [29].

The minima in the pair potential  $V(r)$  (Fig. 5) are all positive in the high density region (e.g.,  $\bar{\rho} = 4\text{g/cm}^3$ ), with  $N_c \sim 10$  or more. The next lower density region develops a deeper first minimum and negative secondary minima. The third region (e.g.  $\bar{\rho} = 3.3\text{g/cm}^3$ ) pulls in ions to the center by making the secondary minima less attractive. In the lowest density region the first minimum becomes very deep, and eventually becomes negative enough to form persistent covalent bonding.

The NPA calculation is for a uniform fluid where the  $2k_F$  scattering is tightly linked to the liquid structure and the coordination number through the Friedel minima in the pair potential that correlate the whole fluid. Density fluctuations near a phase transition become very long ranged. Large- $N$  QMD simulations may be necessary to recover such effects. If not, the sharp transition gets ‘rounded off’, unless at least one phase is a crystalline solid. It is hypothesized that  $l$ -carbon passes from a uniform fluid to a higher-density uniform fluid at  $3.5\text{g/cm}^3$  LPT which is a first-order transition. The LPTs at  $3.15$  and  $3.75\text{g/cm}^3$  show discontinuities only in the compressibility. They may involve narrow amorphous intermediates bridging uniform phases, since the QMD pressure distributions at these LPTs fit to two Gaussians.

In conclusion, the ionic and electronic structure of  $l$ -carbon can be accurately modeled as that of a uniform *liquid metal* whose structure is dominated by strong electron-ion interactions at the Fermi surface. We find three liquid-liquid phase transition at  $1\text{eV}$  in the range  $2.9\text{-}4.0\text{g/cm}^3$  studied in detail here, as confirmed by both NPA and QMD calculations.

## Appendix

Supplemental Material in support of the main text titled: A ‘simple metal’ description of liquid carbon, its warm-dense matter states, and the identification of liquid-liquid phase transitions.

Here we use the same abbreviations, acronyms and units (Hartree atomic units) as defined in the main text. This supplemental material (SM) deals with the following topics.

- (i) Details of the QMD-SCAN calculations used in this study
- (ii) The Gaussian distributions for QMD-SCAN estimates of the equilibrated pressure.
- (iii) One-atom density functional theory used in the NPA
- (iv) The linear-response (LR) potentials and the electron response function used in the NPA method.
- (v) Examination of the origin of discontinuities in the pressure.
- (vi) The electrical conductive of liquid carbon.

*Details of the QMD-SCAN calculations used here.*

We have used finite- $T$  DFT-MD (QMD) calculations where classical molecular dynamics is used to evolve 108 ions in a cubic simulation cell, while the electrons, with four ionized electrons per carbon atom are treated quantum mechanically using density functional theory. The numerical code implemented in the Vienna ab initio simulation package VASP 5.4.4 [25], and the projector augmented wave pseudopotential for the interaction between the nuclei and the electrons provided in VASP were used. The exchange and correlation potential is approximated by the SCAN functional which has been found to perform better for systems with covalent interactions [26]. The simulations used an energy cutoff of 414 eV and a simulation time of 4 ps. The ion temperature was controlled with a Nosé thermostat, and enough empty bands were included to ensure that the highest energy bands had negligible occupations. Evaluations of the Brillouin zone were performed at the Baldereschi  $k$ -point [39].

*The Gaussian distributions for QMD-SCAN estimates of the equilibrium pressure.*

Since the evidence for the LPTs are to be based on breaks in the predicted pressure, particular care was used to determine the equilibrium pressure from the simulation in a consistent, non-subjective manner. The QMD simulation records a distribution of pressures around the thermodynamic mean value, and they form a Gaussian distribution for a uniform fluid at equilibrium. Hence the simulation data were fitted to a Gaussian and the most probable pressure was determined from the peak of the Gaussian. In two cases, viz., near the LPT<sub>3</sub> and LPT<sub>3.75</sub>, an average over two Gaussians seemed more appropriate. This is illustrated in Figs. 6 and 7.

The pressure evaluated in this manner, using the SCAN XC-functional is plotted as SCAN-P in Fig. 3(b) of the main text. The width of the unnormalized Gaussian distribution,  $\Delta P$  is used to characterize the density fluctuations in the system and displayed in panel (b) of Fig. 3 of the main text, and labeled SCAN- $\Delta P$ . Using the fit form  $f(p) = a \exp\{-w^2(p - p_m)^2\}$  for the frequency of occurrence of the pressure,  $p_m$  is the mean pressure, while  $w$  was taken as a measure of the width of the distribution. The width has been multiplied by a

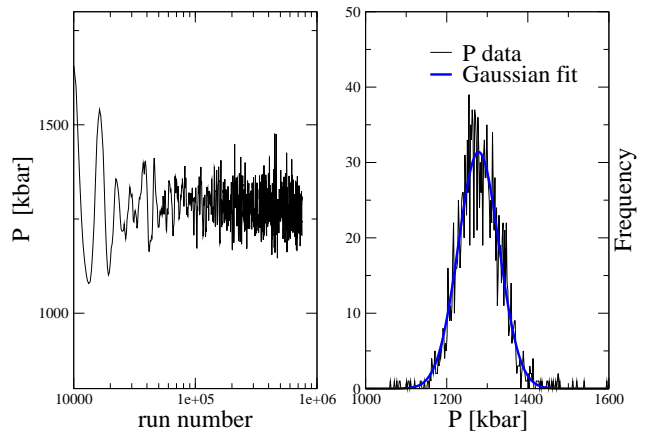


FIG. 6. (Color online) (a) Pressure ‘readings’ at 1 eV from a DFT-MD simulation using 108 atoms at 3.1 g/cm<sup>3</sup> very close to the LPT<sub>3</sub>. The ‘run number’ is an arbitrary index. (b) The pressure ‘readings’ are fitted to a Gaussian (unnormalized), and the equilibrium pressure is taken to be that corresponding to the maximum of the Gaussian. In the present case a bimodal character is clear and a sum of two Gaussians with weights of 0.699 and 0.301 is appropriate, as in Fig. 4 of the main text.

factor of 3.3 in order to plot it in the same range as the other curves.

*The one-atom density functional theory used in the NPA.* Detailed discussions of the NPA may be found in several recent publications [28, 33], besides some of the earlier publications [30–32]. In this study, the density  $\bar{\rho}$ , and temperature  $T$  (in energy units) are such that the carbon atom is found to carry only the 1s shell of bound electrons, providing a very simple model of an atom in a plasma. Hence, for simplicity of discussion we develop the two coupled DFT equations, i.e., for electrons and for the ions that are solved in the NPA, in the following simplified form where Hartree atomic units ( $|e| = \hbar = m_e = 1$ ) are employed.

In our ‘one-atom’ DFT model, coupled equations resulting from the stationary condition of the grand potential  $\Omega(n, \rho)$  considered as a functional of the one body electron and ion densities  $n(r), \rho(r)$  are solved. A single carbon nucleus is taken as the origin, and immersed in the electron and ion distributions of the fluid, forming the system to be considered. Initially, suitable trial values of  $n(r)$  and  $\rho(r)$  are assumed. The coupled equations are:

$$\delta\Omega [n, \rho] / \delta n = 0 \quad (\text{A.1})$$

$$\delta\Omega [n, \rho] / \delta \rho = 0 \quad (\text{A.2})$$

where the functional derivatives are implied. The first of these reduces to the familiar Kohn-Sham equation for the electron density around the nucleus, while the second reduces to a classical DFT equation for the ion distribution.

A bare carbon nucleus of charge  $Z_n$  is the origin

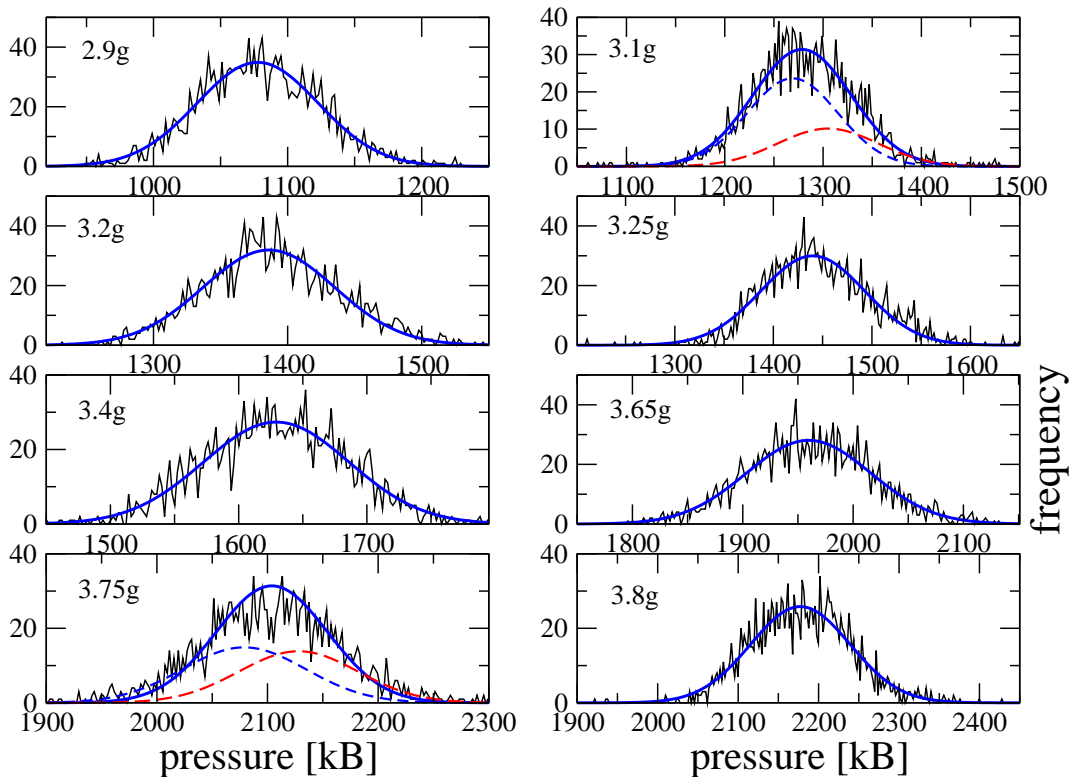


FIG. 7. (Color online) (a) Pressure ‘distributions’ at 1 eV fitted to Gaussians. The distributions at LPT<sub>3</sub> and LPT<sub>3.75</sub> use a two-Gaussian fit. Although there is a discontinuity in the QMD-SCAN pressure at 3.42g/cm<sup>3</sup>, the  $P$  distribution at 3.4g/cm<sup>3</sup> shows no clear tendency to a bimodal distribution

of coordinates of the uniform system of electrons and ions. Spherical symmetry is applicable, as we consider a uniform fluid. The inhomogeneous densities  $n(r), \rho(r)$  around the carbon nucleus become the ‘bulk’ densities  $\bar{n}, \bar{\rho}$  at large distances  $r \rightarrow R_c$ , where  $R_c$  is the about ten Wigner Seitz (WS) radii. A shorter  $R_c \sim 5r_{ws}$  can be used at higher temperatures. Here  $r_{ws}$  is given by  $r_{ws} = \{3/(4\pi\bar{\rho})\}^{1/3}$ . Thus, unlike in average-atom (AA) models where the electrons of an ion are confined to the WS-sphere within which the Kohn-Sham equation is solved, the NPA uses the large ‘correlation sphere’ of radius  $R_c$  in solving the DFT equations. The pair-distribution functions (PDFs)  $g_{ab}(r), a = e, i$  refer to electrons or ions and describe the structure of the environment where the carbon atom is placed. Then

$$\rho(r) = \bar{\rho}g_{ii}(r), \quad n(r) = \bar{n}g_{ei}(r) \quad (\text{A.3})$$

The PDF  $g_{ii}(r)$  will be referred to as  $g(r)$  for brevity. The grand potential can be written as

$$\Omega = T[N, \rho] + \Omega_e + \Omega_{ei} + \Omega_i. \quad (\text{A.4})$$

Here  $T[n, \rho]$  is the kinetic energy functional of a *noninteracting* system having the exact interacting densities. A simplified form for  $\Omega_e$  is given below merely for ease of presentation, assuming a point ion-model  $U_{ei}(r) = -\bar{Z}/r$  for the electron-ion interaction. The ion contribution  $\Omega_i$

is also discussed below. The more complete model, applicable even to ion mixtures is found in Refs. [30, 31] and used in the computations .

$$\begin{aligned} \Omega_e = & - \int d\mathbf{r} \frac{Z_n}{r} n(r) + \frac{1}{2} \int d\mathbf{r} d\mathbf{r}' \frac{n(r)n(r')}{|\mathbf{r} - \mathbf{r}'|} \\ & + \int d\mathbf{r} F_{ee}^{xc}[n] - \mu_e \int d\mathbf{r} n(\mathbf{r}), \end{aligned} \quad (\text{A.5})$$

$$\Omega_{ei} = - \int d\mathbf{r} d\mathbf{r}' \frac{\bar{Z}\rho(r)n(r')}{|\mathbf{r} - \mathbf{r}'|} + \int d\mathbf{r} F_{ei}^{xc}[n, \rho] \quad (\text{A.6})$$

Note that three-body and higher contributions beyond pair interactions are all contained in the XC-functionals, and are *not* neglected in the theory. The one-atom DFT approach (viz., the NPA) does not use an  $N$ -center potential energy surface due to the ions for the Kohn-Sham electrons, as is the case with the  $N$ -atom DFT deployed in VASP [25] and similar codes. What we have is the appropriate one-atom mapping of the  $N$ -atom DFT calculation.

We have used in Eq. A.5 a point-ion model  $-\bar{Z}/r$  for the electron-ion interaction of the field ions only for simplicity of presentation. In actual calculations a local pseudopotential  $U_{ei}(q) = -\bar{Z}V_q M_q$ , where  $V_q = 4\pi/q^2$  and a form factor  $M_q$  are used. The form factor, and the corresponding ion-ion pair potential are also determined self-consistently from the NPA, as discussed elsewhere [28, 30, 31]. Non-local forms of the pseudopotential

TABLE I. . The pressure at 1 eV without (labeled no B) and with (labeled with B) bridge corrections, and the corresponding hard-sphere packing fraction  $\eta$  for selected densities.

$\rho$ g/cm <sup>3</sup>	3.0	4.0	8.0
$P$ TPa, no B	0.03413	0.1705	1.540
$P$ TPa, with B	0.03359	0.1700	1.538
$\eta$	0.1080	0.2030	0.3515

have not been found necessary for NPA calculations for uniform-density warm dense fluids or for cubic solids.

The ion contribution  $\Omega_i$ , though not displayed with the equations, can be obtained from the above equations by appropriately replacing  $n(r)$  by  $\bar{Z}\rho(r)$  if the ion-electron interaction is modeled by point ions, while also replacing  $F^{xc}$  contributions appropriately. The electron-ion xc-functional  $F_{ei}^{xc}$  is usually neglected in most NPA calculations, being largely equivalent to making the Born-Oppenheimer approximation, and neglecting certain correlation corrections of the form  $\langle n(\mathbf{r})\rho(\mathbf{r}') \rangle - \langle n(r) \rangle \langle \rho(r') \rangle$ . This is equivalent to using a ‘random-phase’ approximation for the electron-ion response function. This is appropriate for dense uniform fluids of carbon studied here. However, such correlations may be important at low densities, and with composite carbon grains and amorphous systems.

The stationary condition on  $\Omega$  under functional variation  $\delta n$  leads to the usual Kohn-Sham (KS) equation for electrons moving in an effective potential  $U_e(r)$ . Functional differentiation with respect to  $\delta\rho$  leads to an equation identifiable with the modified hyper-netted-chain (MHNC) equation if the ion-ion XC-functional is identified with the hyper-netted-chain (HNC) diagrams and bridge diagrams used for classical systems. The ions are classical in the regime of study, and there is no exchange contribution. Then the effective classical KS potential for the ions can be identified with the ‘potential of mean force’,  $U_{ii}(r)$  (see Sec. III of Ref. [32]) of classical statistical mechanics.

The bridge contributions can be included using the hard-sphere model, with the hard sphere packing fraction parameter  $\eta$  selected using the Lado-Foils-Ashcroft criterion [40]. We find that the inclusion of bridge corrections has only a negligible effect for  $l$ -carbon in the range of  $\bar{\rho}, T$  studied here. Typical values are given below

In solving the Kohn-Sham equation, the field ion distribution  $\rho(r) = \bar{\rho}g(r)$  occurring in  $\Omega_e(r), \Omega_{ei}(r)$  as well as in the corresponding KS equation  $\delta\Omega/\delta n$  is replaced by  $\bar{\rho}g_{cav}(r)$ , where  $g_{cav}(r)$  is a model ion-ion PDF which is just a spherical cavity of radius  $r_{ws}$ . Hence solving the electron KS equation coupled to the ion KS equation is much simplified, and the only parameter associated with the ion distribution that has to be varied self-consistently is the ion Wigner-Seitz radius  $r_{ws}$  appropriate to a given free electron density  $\bar{n}$  given as the input.

Thus the primary input variable is the free electron density, for a given temperature and nuclear charge. The equilibrium ion density  $\bar{\rho}$  is determined for each given  $\bar{n}$  in this manner, while solving the electron KS equation self-consistently, starting from a trial  $n(r)$  and  $\bar{Z}$ . At the end of the calculation, the effect of the cavity distribution is subtracted off using linear response theory. This provides us the nonlinear response (Kohn-Sham electron density) of an interacting uniform electron fluid to the carbon ion with its set of bound electrons.

The self-consistent solution for the continuum and bound state solutions is constrained to satisfy the Friedel sum rule and verified for satisfying the  $f$ -sum rule. The xc-functional used for the electron KS equation is the finite- $T$  xc-functional of Perrot and Dharma-wardana [41] within the local density approximation (LDA). The xc-functional depends on  $T/E_F$ , where  $E_F$  is the Fermi energy of the free electrons. The electron system is a strongly degenerate quantum gas in the system under study. A comparison of the finite- $T$  xc-functional used here with the parametrization due to Dornheim *et al.* [42] fitted to quantum Monte Carlo data showed good agreement [43].

This partial decoupling of the electron Kohn-Sham equation and the ion Kohn-Sham equation used in the NPA implementation is possible because the electron Kohn-Sham equation is found to be only weakly dependent on the details of  $g_{ii}(r)$  for  $r > r_{ws}$ . As already noted, we use the free electron part of  $n(r)$ , viz.,  $n_f(r) = \bar{n} + \Delta n_f(r)$  obtained from the KS equation to construct the  $\Delta n_f(r)$  that would be obtained if there were no  $g_{cav}(r)$ , using linear response (LR) theory. The corrected  $\Delta n_f(r)$  is the response of a uniform electron fluid (in the presence of a non-responding neutralizing uniform ion background) to the carbon ion of charge  $\bar{Z}$ . Hence this corrected  $\Delta n_f(r)$  may be regarded as being independent of the assumed form of  $g(r)$  in solving the electron KS equation, as long as it satisfied basic criteria in regard to charge neutrality and the perfect screening sum rule.

Once the electron Kohn-Sham equation is solved using  $g_{cav}(r)$ , we already have the three quantities  $\bar{n}, \bar{Z}$  and hence  $\bar{\rho}$ . We also have the KS eigenfunctions  $\phi_\nu(r)$  and eigenvalues  $\epsilon_\nu$ , with  $\nu = n, l$  for bound states, and  $\nu = k, l$  for continuum states, with  $\epsilon_k = k^2/2$ , together with the phase shifts  $\delta_{kl}$ . These satisfy the Friedel sum rule and the simple charge neutrality condition  $\bar{n} = \bar{Z}\bar{\rho}$ .

*The linear response (LR) function of the electron fluid and its use in calculating the pseudopotential.* The KS calculation for the electron states for the NPA in a fluid involves solving a simple radial equation. The continuum states  $\phi_{k,l}(r), \epsilon_k = k^2/2$ , with occupation numbers  $f_{kl}$ , are evaluated to a sufficiently large energy cutoff and for an appropriate number of  $l$ -states (typically 9 to 39 were found sufficient for the calculations presented here). The very high- $k$  contributions are included by a Thomas-Fermi correction. This leads to an evaluation

of the free-electron density  $n_f(r)$ , and the free-electron density pileup  $\Delta n'(r) = n_f(r) - \bar{n}$ . A part of this pileup is due to the presence of the cavity potential. This contribution  $m(r)$  is evaluated using its linear response to the electron gas of density  $\bar{n}$  using the interacting electron response  $\chi(q, T_e)$ . The cavity corrected free-electron pileup  $\Delta n_f(r) = \Delta n'(r) - m(r)$  is used in constructing the electron-ion pseudopotential as well as the ion-ion pair potential  $V_{ii}(r)$  according to the following equations (in Hartree atomic units), given for Fourier-transformed quantities:

$$U_{ei}(k) = \Delta n_f(k)/\chi(k, T_e), \quad (\text{A.7})$$

$$\chi(k, T_e) = \frac{\chi_0(k, T_e)}{1 - V_k(1 - G_k)\chi_0(k, T_e)}, \quad (\text{A.8})$$

$$G_k = (1 - \kappa_0/\kappa)(k/k_{\text{TF}}); \quad V_k = 4\pi/k^2, \quad (\text{A.9})$$

$$k_{\text{TF}} = \{4/(\pi\alpha r_s)\}^{1/2}; \quad \alpha = (4/9\pi)^{1/3}, \quad (\text{A.10})$$

$$V_{ii}(k) = Z^2 V_k + |U_{ei}(k)|^2 \chi_{ee}(k, T_e). \quad (\text{A.11})$$

Here  $\chi_0$  is the finite- $T$  Lindhard function,  $V_k$  is the bare Coulomb potential, and  $G_k$  is a local-field correction (LFC). The finite- $T$  compressibility sum rule for electrons is satisfied since  $\kappa_0$  and  $\kappa$  are the non-interacting and interacting electron compressibilities respectively, with  $\kappa$  matched to the  $F_{xc}(T)$  used in the KS calculation. In Eq. A.10,  $k_{\text{TF}}$  appearing in the LFC is the Thomas-Fermi wavevector. We use a  $G_k$  evaluated at  $k \rightarrow 0$  for all  $k$  instead of the more general  $k$ -dependent form (e.g., Eq. 50 in Ref. [41]) since the  $k$ -dispersion in  $G_k$  has negligible effect for the WDMs of this study. The xc-functional is used in the LDA which is efficient and accurate because the one-center electron density  $n(r)$  is smooth compared to the complex  $N$ -center electron density used in VASP-type  $N$ -center DFT calculations.

*Examination of the origin of discontinuities in the pressure.*

It is known that average-atom (AA) models [21] that confine all the bound and free electrons associated with an ion in the Wigner Seitz sphere can produce spurious discontinuities in the pressure and in the mean ionization  $\bar{Z}$ . In the NPA the electrons are not confined to the WS-sphere, but to the correlation sphere of radius  $R_c \sim 10r_{\text{ws}} - 5r_{\text{ws}}$ . Average atom models have to deal with electrons that “leak out” of the WS-sphere, and model dependent effects arising from the choice of boundary conditions at the surface of the WS-sphere; these do not arise in the NPA.

However, NPA models as well as AA models have to deal with discontinuities that arise when a well-confined bound state moves upwards in energy and into the continuum due to changes in density or temperature. In some cases, such ionization is accompanied by phase transitions and discontinuities in physical properties. In other cases, when unphysical discontinuities occur, they can be corrected by ensuring that appropriate discontinuities that cancel them are properly included in the xc-functionals. However, we have no changes in the degree of ionization

( $\bar{Z}$ ) or any other critical parameters in the range of densities studied here, and hence no spurious discontinuities are expected in this range of  $\bar{\rho}, T$ .

The NPA pressure is obtained from an evaluation of the Helmholtz free  $F$  of the system. This consists of contributions of the form [30, 31]:

$$F = F_e^0 + F_e^{xc} + F_{em}^a + F_{em}^b + F_{12} + F_I^0. \quad (\text{A.12})$$

The first two terms deal with the free energy of the non-interacting uniform electron fluid and its finite- $T$  exchange-correlation energy at the given density and temperature  $T$ . The last term,  $F_I^0$  is the ideal (classical) free energy of the ion subsystem. The third and fourth terms together form the embedding energy of the nucleus and the inhomogeneous electron density that form neutral pseudo-atom in the uniform electron fluid. The fifth term,  $F_{12}$  contains the interactions between pseudoatoms brought in via the pair-potential, pair-distribution functions and the ion-ion correlation effects. The contribution to the pressure from all the terms except  $F_{12}$  can be expressed analytically. The density derivative of the term  $F_{12}$  has to be evaluated numerically. Then the pressure can be written as:

$$P = P_e^0 + P_e^{ex} + P_{em}^a + P_{em}^b + P_{12} + P_I^0. \quad (\text{A.13})$$

No discontinuities are expected in  $P_e^0, P_e^{ex}$  or  $P_I^0$  when treated as a function of  $\bar{\rho}$  as the number of free electrons per ion,  $\bar{Z}$  remains constant at a value of four in this density range. Hence, in Fig. 8, panel (a) we display only the two components of the embedding energy and the pair-interaction free energy  $F_{12}$  as a function of the density, at 1 eV. In order to understand the physical content of the embedding pressure ([31]) we write down the potential that produces a single neutral pseudo atom in the uniform fluid of mean electron density  $\bar{n}$  and mean ion density  $\bar{\rho}$ , viz.,

$$V^{npa} = \frac{1}{r} \star (-\bar{Z}\delta_0 + \nu + \Delta n). \quad (\text{A.14})$$

Here  $\bar{Z}\delta_0$  defines the nuclear term at the origin, while  $\nu(r)$  is the density of the spherical cavity which mimics the ion distribution  $\rho(r)$  by  $\bar{Z}g_{cav}(r)$ .

$$\nu(r) = \bar{n}, r > r_{\text{ws}}, \text{ else } \nu(r) = 0. \quad (\text{A.15})$$

Also,  $\Delta n$  is the displaced electron density with reference to the mean electron density  $\bar{n}$ . The symbol  $\star$  defines a convolution product. We also define the integration over all space via the symbol  $\circ$ .

$$f \star g = \int f(\vec{r})g(\vec{r} - \vec{s})d\vec{s} \quad (\text{A.16})$$

$$f \circ g = \int f(r)g(r)d\vec{r}. \quad (\text{A.17})$$

The volume are over a sphere of radius  $R_c \sim 10r_{\text{ws}}$ . Then, denoting the volume of the Wigner-Seitz sphere

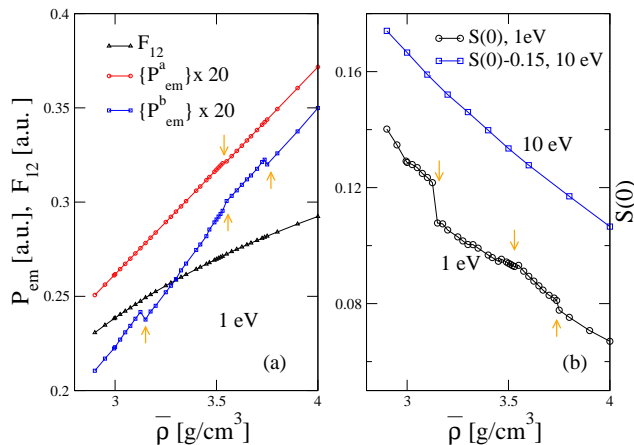


FIG. 8. (Color online) (a) We display the two components of the embedding pressure obtained without numerical differentiation from the embedding free energy of the neutral pseudo atom. The pair-interaction free energy  $F_{12}$  which contains bonding effects and many-ion correlation effects is also displayed. The embedding pressure component  $P_{em}^b$  displays three discontinuities, while  $F_{12}$  shows a slight discontinuity near  $\bar{\rho} = 3.52$ . (b) We display the  $k \rightarrow 0$  limit of the structure factor which is  $S(0) = \kappa/\kappa_0$ , where  $\kappa_0, \kappa$  are the ideal fluid compressibility of the ions, and the interacting compressibility respectively. The value of  $S(0)$  at 10 eV is shifted by 0.15 for ease of comparison, and shows no discontinuities. Similarly, the pressure at 10 eV, displayed in the Fig.3(a) of the main text, shows no discontinuities.

by  $\Omega_{ws}$ , the two embedding pressure terms can be written as [31]:

$$P_{em}^a = (\nu - \bar{n}) \circ V^{npa} / \Omega_{ws} \quad (\text{A.18})$$

$$P_{em}^b = -\bar{Z} V^{npa}(r_{ws}). \quad (\text{A.19})$$

Since  $\bar{Z} = 4$ , and remains at that value through out the range of densities studied, the discontinuities in the embedding pressure are caused solely by the ‘external potential’ associated with the creation of the carbon pseudoatom, and not associated with bonding with other carbon ions (such contributions are in  $F_{12}$ ).

This re-enforces our conclusion that the observed LPTs are associated with changes in coordination number  $N_c$  and the effect on the electron-ion interactions at the Fermi energy via  $q = 2k_F$  scattering. The coordination number  $N_c$  can be approximately determined from the area under the first peak of  $g(r)$ , and has been reported in detail by Vorberger *et al* [5]. They do not cause discontinuities in  $P$  but clearly cause discontinuities in the compressibility (as seen in  $S90$ ), i.e., a derivative of the pressure.

#### The electrical conductivity of liquid carbon.

The static electrical conductivity  $\sigma$  usually changes at phase transitions because at least one of several physical parameters change abruptly. These are the number of free carriers, the distribution of the ions that cause the scattering of electrons, and the scattering potential.

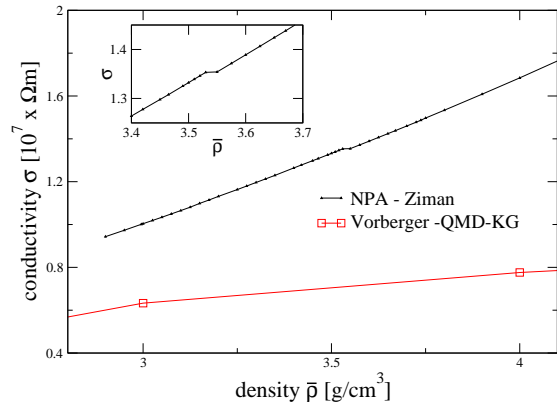


FIG. 9. (Color online) The conductivity calculated using the NPA pseudopotential  $U_{ei}(k)$  and the structure factor  $S(k)$  in the Ziman formula is displayed. The conductivity results reported by Vorberger *et al.* is also displayed. The slight discontinuity in  $\sigma$  at  $\approx 3.53\text{g/cm}^3$  is shown in more detail in the inset. The discontinuity coincides with the LPT<sub>3.5</sub>. The conductivity shows no discernible discontinuities at the other two LPTs.

These properties are contained in the pseudopotential  $U_{ei}(k)$ , the structure factor  $S(k)$  and the screening function of the system, when considering the static conductivity.

In the present case  $\bar{Z}$  remains unchanged at four. The high value of the Fermi energy  $E_F$  of liquid carbon, e.g., 28.8 eV near the diamond density of 3.5 g/cm<sup>3</sup>, implies that at 1 eV the electrons are nearly completely degenerate, and hence electron scattering can occur only from one edge of the Fermi surface to the other, with a momentum transfer  $q = 2k_F$ , where  $k_F$  is the Fermi momentum. Thus the quantities  $U_{ei}(2k_F)$ ,  $S(2k_F)$  and the inverse dielectric function at  $2k_F$  which screens the pseudopotential determine the electrical conductivity. We noted that, due to the strong electron-ion scattering at  $2k_F$ , the structure factor remains tied to a peak at  $2k_F$ . Thus sharp changes are not expected in the electrical conductivity of this system under the liquid-liquid phase transitions. However, an extremely weak discontinuity can be seen (Fig. 9) at the LPT<sub>3.5</sub>, i.e., at the nominal diamond density where we also noted a discontinuity in the pressure calculated via QMD-SCAN, and via the NPA model. Given the very small magnitude of the discontinuity in  $\sigma$ , it is not surprising that no discontinuities in  $\sigma$  are seen at LPT<sub>3</sub> and LPT<sub>3.75</sub> where the pressure isotherm also did not show any discontinuities.

The QMD estimate of the conductivity of liquid carbon is approximately half that of the NPA-Ziman estimate. This difference becomes even larger at higher densities, and may be associated with the fact that the NPA model assumes a strictly homogeneous fluid, while the QMD simulation considers the fluid to be an average over

many realizations of a large variety of inhomogeneous atomic clusters. While such averaging is effective when the ions themselves actually easily form a uniform system, it is not evidently so in systems where there is transient bonding as well as incipient formation of preferred clusters dictated by the tetrahedral character of the fluid. Hence, when such systems form homogeneous fluids, the

QMD simulation may need a large number of atoms. On the other hand, if the fluid is truly a dispersed phased of atomic clusters, the NPA approach that assumes a uniform-density fluid cannot accurately describe such a system using the simple ion-ion xc-functionals based on the Ornstein-Zernike and the modified HNC approach (i.e., HNC+bridge) used here.

- 
- [1] G. Galli, R. Martin, R. Car, and M. Parrinello, Phys. Rev. Lett. **63**, 988 (1989).
- [2] I. Štich, R. Car, and M. Parrinello, Phys. Rev. Lett. **63**, 2240 (1989).
- [3] J. N. Glosli and F. H. Ree, Phys. Rev. Lett. **82**, 4659 (1999).
- [4] Luca M. Ghiringhelli, Jan H. Los, A. Fasolino, and Evert Jan Meijer, Phys. Rev. B **72**, 214103, (2005).
- [5] J. Vorberger, K.U. Plageman, R. Redmer, High Energy Density Physics **35**, 100737 (2020)
- [6] H. D. Whitley, D. M. Sanchez, S. Hamel, A. A. Correa, and L. X. Benedict, Contrib. Plasma Phys. **55**, 390 (2015)
- [7] D. Kraus, J. Vorberger, D. O. Gericke, V. Bagnoud, A. Blazevic, W. Cayzac, A. Frank, G. Gregori, A. Ortner, A. Otten, F. Roth, G. Schaumann, D. Schumacher, K. Siegenthaler, F. Wagner, K. Wunsch, and M. Roth, Phys. Rev. Lett. **111**, 255501 (2013).
- [8] S. Hamel, Lorin X. Benedict, Peter M. Celliers, M. A. Barrios, T. R. Boehly, G. W. Collins, Tilo Döppner, J. H. Eggert, D. R. Farley, D. G. Hicks, J. L. Kline, A. Lazicki, S. LePape, A. J. Mackinnon, J. D. Moody, H. F. Robey, Eric Schwegler, and Philip A. Sterne, Phys. Rev. B **86**, 094113 (2012).
- [9] M. W. C. Dharma-wardana and F. Perrot, Phys. Rev. Lett., **65**, 76 (1990).
- [10] J. D. Lindl, P. Amendt, R. L. Berger, S.G. Glendinning, S. H. Glenzer, S.W. Haan, R. L. Kauffman, O. L. Landen, and L. J. Suter, Phys. Plasmas **11**, 339 (2004).
- [11] L. X. Benedict, K. P. Driver, S. Hamel, B. Militzer, T. Qi, A. A. Correa, A. Saul, E. Schwegler, Phys. Rev. B **89** 224109 (2014).
- [12] W. B. Hubbard, W. J. Nellis, A. C. Mitchell, N. C. Holmes, S. S. Limaye, and P. C. McCandless, Science **253**, 648 (1991).
- [13] A. Y. Potekhin, G. Massacrier, and G. Chabrier, Phys. Rev. E **72**, 046402 (2005)
- [14] B. L. Sherman, H. F. Wilson, D. Weeraratne, and B. Militzer, Phys. Rev. B **86**, 224113 (2012).
- [15] K. P. Driver and B. Militzer, Phys. Rev. Lett. **108**, 115502 (2012).
- [16] F.H. Stillinger and T. A. Weber, Phys. Rev. B **31**, 5262-5271 (1985)
- [17] F. Ercolessi and J. B. Adams, Europhysics Letters, **26**, 583 (1994)
- [18] L. Li and R. G. Parr, The Journal of chemical physics, **84**, 1704 (1986).
- [19] Mandy Bethkenhagen, Bastian B. L. Witte, Maximilian Schörner, Gerd Röpke, Tilo Döppner, Dominik Kraus, Siegfried H. Glenzer, Philip A. Sterne, and Ronald Redmer, Phys. Rev. Research **2**, 023260 (2020).
- [20] Balas F. Rosznyi, High Energy Density Physics **4**, 64 (2008)
- [21] M. S. Murillo, J. Weisheit, S. B. Hansen, and M. W. C. Dharma-wardana, Phys. Rev. E **87**, 063113 (2013).
- [22] J. P. Perdew, K. Burke, and M. Ernzerhof, Phys. Rev. Lett. **77**, 3865 (1996).
- [23] Christine J. Wu, James N. Glosli, Giulia Galli, and Francis H. Ree, Phys. Rev. Lett. **89**, 135701 (2002)
- [24] X.Gonze and C. Lee, Computer Phys. Commun. **180**, 2582-2615 (2009).
- [25] G. Kresse and J. Furthmüller, Phys. Rev. B **54**, 11169 (1996).
- [26] Richard C. Remsing, Michael L. Klein and Jianwei Sun, Physical Review B **96** 024203 (2017)
- [27] J. Sun, B. Xiao, Y. Fang, R. Haunschild, P. Hao, A. Ruzsinszky, G. I. Csonka, G. E. Scuseria, and J. P. Perdew, Phys. Rev. Lett. **111**, 106401 (2013).
- [28] Lucas J. Stanek, Raymond C. Clay III, M. W. C. Dharma-wardana, Mitchell A. Wood, Kristian R. C. Beckwith, and Michael S. Murillo, Phys. Plasmas **28**, 032706 (2021) <https://arxiv.org/abs/2012.06451>
- [29] Supplemental material supporting this publication. It deals with the following topics. (i) Details of QMD-SCAN calculations used in this work, (ii) Gaussian distributions for the pressure obtained from QMD-SCAN studies. (iii) One-atom DFT used in the NPA method. (iv) Linear response potentials and the electron response function used in NPA theory. (v) Examination of the origin of discontinuities in the pressure. (vi) The electrical conductivity of *l*-carbon.
- [30] F. Perrot and M.W.C. Dharma-wardana, Phys. Rev. E. **52**, 5352 (1995)
- [31] F. Perrot, Phys. Rev. E **47**, 570 (1993).
- [32] M. W. C. Dharma-wardana and F. Perrot, Phys. Rev. A **26**, 2096 (1982)
- [33] M.W.C. Dharma-wardana, Dennis D. Klug, and Richard C. Remsing, Phys. Rev. Lett. **125**, 075702 (2020) doi: 10.1103/PhysRevLett.125.075702
- [34] M. W. C. Dharma-wardana, Physics of Plasmas **28**, 052108 (2021); <https://doi.org/10.1063/5.0047642>
- [35] B. Darwent, *National Standard Reference Data Series*, National Bureau of Standards, No. 31, Washington, DC, 1970; [http://www.wiredchemist.com/chemistry/data/bond\\_energies\\_le](http://www.wiredchemist.com/chemistry/data/bond_energies_le)
- [36] M. W. C. Dharma-wardana, Phys. Rev. E **86**, 036407 (2012).
- [37] M. W. C. Dharma-wardana, Contrib. Plasma Phys. **58** 128-142 (2018)
- [38] M. van Thiel, F.H. Ree, Phys. Rev. B **48** 2591, (1993)
- [39] A. Baldereschi, Phys. Rev. B, **7**, 5212 (1973)
- [40] F. Lado, S. M. Foiles and N. W. Ashcroft, Phys. Rev. A **26**, 2374 (1983).
- [41] F. Perrot and M. W. C. Dharma-wardana, Phys. Rev. B

- 62**, 16536 (2000); *Erratum*: **67**, 79901 (2003); arXiv:1602.04734.
- [42] Tobias Dornheim, Simon Groth, Michael Bonitz *Physics Reports*, **744**, 1-86 (2018), <https://doi.org/10.1016/j.physrep.2018.04.001>.
- [43] M. W. C. Dharma-wardana, *Phys. Rev. B* **100**, 155143 (2019) DOI: 10.1103/PhysRevB.100.155143